Numerical modeling of generation and propagation of Görtler vortices

Prof. Dr. Andrey Boiko

Dr. Kirill Demyanko

Prof. Dr. Dmitri Kuzmin

Dr. Otto Mierka

Prof. Dr. Yuri Nechepurenko

Dr. Ludmila Rivkind[1]

Technische Universität Dortmund

Fakultät für Mathematik, Lehrstuhl III

Vogelpothsweg 87, 44227 Dortmund

[1]Department of Mathematical Information Technology, University of Jyväskylä, P.O. Box 35 (Agora), FI-40014, Jyväskylä, Finland

Abstract

Complementary to a recent experimental study on local generation and propagation of Görtler vortices, direct numerical simulations of wind-tunnel experiments were performed to study stability characteristics of laminar subsonic flows of viscous incompressible fluids. This report describes various computational aspects and numerical methods implemented the finite element software package FEATFLOW which was used to solve the incompressible Navier-Stokes equations in this project.

1 Introduction

There is an urgent need for efficient and handy software for three-dimensional numerical simulation of experiments on stability of laminar subsonic shear flows in low-turbulence wind tunnels. Such a software would significantly more accurately assess the adequacy of the experimental data and a design of new fundamental experiments. It would also facilitate the development and verification of various simplified numerical models developed for parametric computations, bridging experimental data, and comparison of effects observed in the experiments with the theoretical results.

However, widespread universal commercial packages designed for simulation of non-stationary flows cannot be used for these purposes directly, because they are not intended for sufficiently precise simulation of evolution of small (in amplitude and extent) flow disturbances. The corresponding extensions of the packages seem only possible if their codes are open-access.

In 2016, a new project aimed at the development and implementation of advanced numerical methods for three-dimensional simulation of wind-tunnel experiments on the stability of laminar shear flows using the open-source FEATFLOW package (http://www.featflow.de/en/index.html) was launched in the framework of cooperation between the Keldysh Institute of Applied Mathematics of the Russian Academy of Sciences, the Khristianovich Institute of Theoretical and Applied Mechanics of the Siberian Branch of the Russian Academy of Sciences, and the Faculty of Mathematics of the TU Dortmund University. To this end, a recent fundamental experiment on excitation of Görtler vortices in a boundary layer over a slightly concave surface by small localized periodic controlled disturbances was chosen [1, 2]. A numerical simulation of the experiment was performed previously using an original simplified linear model based on parabolic equations for generation and propagation of the disturbances. This model was quite adequate for analysis of experimentally observed receptivity of the boundary layer to local nonuniformities of the surface in generating the Görtler vortices and allowed to build a new theory of receptivity based on the so-called optimal disturbances [3]. However, this model did not allow to compute the streamwise component of the disturbance velocity at certain values of parameters under study with a good accuracy, the reasons of this discrepancy still being unknown.

The second and third sections of this report briefly describe the above mentioned wind-tunnel experiment and the simplified numerical model with a focus on discrepancy of their results. The fourth section contains a brief overview of the features of the FEATFLOW package, and discusses problems encountered when using it for three-dimensional simulation of the experiment as well as their possible solutions. Preliminary results given in this section indicate that the FEATFLOW package in the current state is a good starting point to simulate the experiment [1, 2] and apparently other similar experiments, but to reach this goal it requires some additional features, as summarized in the conclusion.

Thus, this report outlines and substantiates the intention to establish a branch of the FEATFLOW package designed for the 3D numerical simulation of experiments on stability of laminar subsonic shear flows in low-turbulence wind tunnels.

2 Wind-tunnel experiment

Görtler instability occurs in a wide range of flow velocities in boundary layers on concave surfaces under the influence of centrifugal force caused by the surface curvature [4]. This instability leads to a formation of streamwise vortices growing downstream, to a dramatic change of heat transfer and skin friction, and to an earlier laminar-turbulent transition, as well as results in other changes in the flow, which are significant in applications. Thus, the problem of excitation and propagation of stationary and non-stationary Görtler vortices is actual for aerodynamic facilities and aircrafts with concave flow-exposed surfaces such as air engine intakes, turbomachine blades, flaps, slats, etc.

Görtler instability has been investigated experimentally, theoretically and numerically for a long time (see reviews in [5–8]). However, the growth of the Görtler vortices predicted by the linear theory of hydrodynamic stability has been observed in a wind-tunnel experiment only recently [5, 9]. A reason for the apparent discrepancy was associated with non-linear effects as the variations of streamwise velocity caused by the vortices were sufficiently large in the experiments (often about 10% of the free-stream velocity, as in [10]). Another reason is related to the so-called transient growth of disturbances in the near-field region of a source of the vortices.

2.1 Experimental setup

The first accurate experimental study of excitation of stationary and non-stationary Görtler vortices by surface nonuniformities localized in the streamwise direction (roughness and vibrations) have only been performed relatively recently [1, 2]. The measurements were carried out in the low-turbulence wind tunnel T–324 of ITAM SB RAS at free-stream velocity $U_\mathrm{e} = 9.18$ m/s, air density $\rho = 1.214$ kg/m^3 and dynamic viscosity $\mu = 1.85 \cdot 10^{-5}$ Pa $\cdot$ c. The free-stream turbulence level in the working part of the wind tunnel did not exceed 0.02% in the frequency range above 1 Hz.

Figure 1 shows the experimental setup in the working part of the wind-tunnel (*1*). The boundary layer under study was created on the concave acrylic plate (*2*), which is 996 mm wide, 2372 mm long, 8 mm thick and has the radius of curvature $R = 8370$ mm. To install a disturbance source, the plate is equipped with an insert (*3*), which is 14 mm long and 157 mm wide. The insert is located 290.3 mm downstream from the leading edge in the central part of the plate. The constant radius of curvature

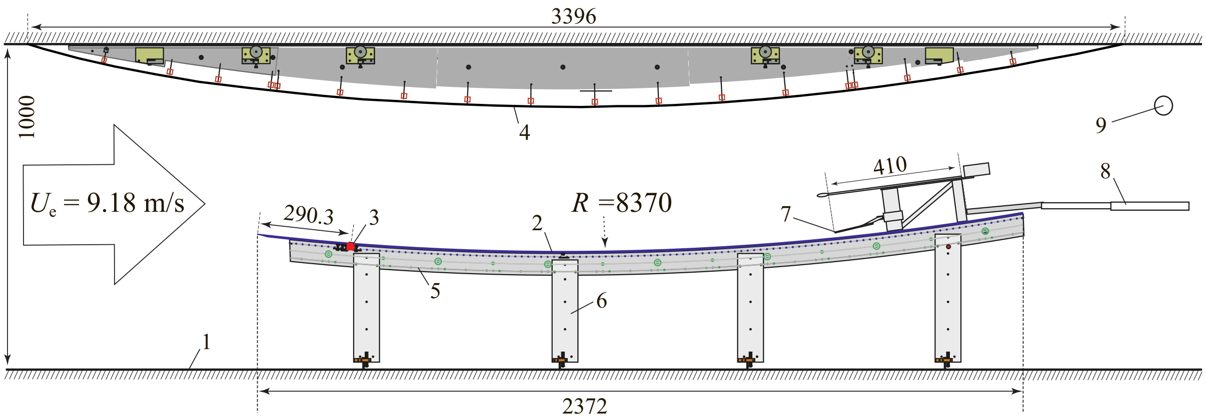

Figure 1: Experimental setup [2]: wall of working part of the wind-tunnel (*1*); concave plate (*2*); the insert for disturbance sources (*3*); adjustable wall bump (*4*); rigid frame made of fixed-radius ribs (*5*); supports (*6*); hot-wire probe with traversing mechanism (*7*); traversing mechanism handle (*8*); flow-blockage adjuster (*9*).

was ensured by a rigid skeleton of a set of bow-shaped dural ribs (*5*), to which the plate was attached thoroughly. The leading edge consists of a circle sector of 6 mm in diameter on the test side smoothly connected to a straight part of 20 mm length on the opposite side of the plate. A required streamwise pressure gradient over the test side of the plates in the region of measurements was achieved by the adjustable wall bump (*4*). The bump and the test plate were located in respect to the wind-tunnel walls in a way to ensure an attached flow near the leading edge of the plate. An additional control over the position of stagnation line was provided by a flow blockage adjuster (a transverse beam downstream of the plate) (*9*). In general, these prerequisites allowed to provide a boundary-layer flow over the concave surface under zero pressure gradient.

The region of measurements was located in the range of the streamwise curved (along the surface of the plate) coordinate $x = 290 \div 1200$ mm. Instantaneous values of the streamwise component of the velocity vector of the flow were measured with a hot-wire (*7*). It was installed on a three-component traversing mechanism (*8*), which allowed to position the wire at any point in the region of measurements with an accuracy of 5 µm in the normal to the surface direction and 200 µm in the streamwise and spanwise directions.

2.2 Disturbance source

To excite three-dimensional controlled vortical disturbances in the boundary layer, a source shown schematically in Fig. 2 was used. The source consists of identical round elastic membranes (*3*) made of latex film with thickness $80 \div 100$ µm located with a constant spacing along the model span. The source was mounted in place of the insert flush with the plate (with accuracy about 1 µm). The membranes were excited with the help of a block of 8 closed woofers, which were located outside of the working part

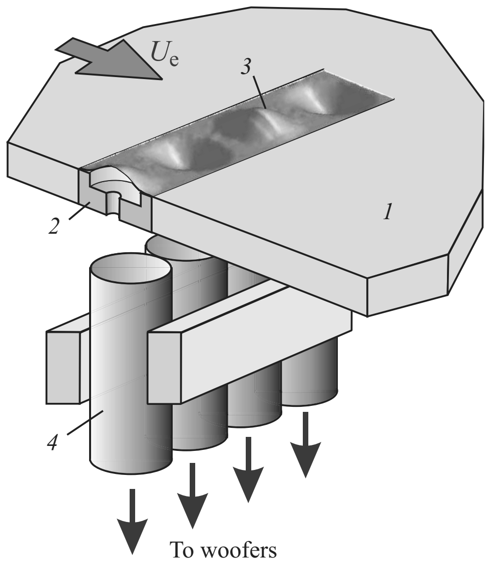

Figure 2: Disturbance source [2]: concave surface (*1*); insert (*2*); elastic membranes (*3*); pneumatic lines (*4*).

of the wind tunnel. The woofers were connected to chambers under the membranes by pneumatic lines (*4*) to create pressure pulsations resulting in membrane oscillations with amplitudes of up to a few tens of microns in the direction normal to the surface. The frequencies, amplitudes, and relative phases of the woofer sinusoidal oscillations were controlled by one of eight channels of electronic part of the source equipped with a special digital-to-analogue converter combined with a power amplifier.

The elastic membranes were glued to the bearing surface of source in a way designed to ensure uniform, small, and constant membrane tension and to isolate the chambers from one another, thus creating a homogeneous set of oscillators along the plate span. The deviation of membrane diameters from one another did not exceed 90 µm, and the variation of amplitudes of membrane oscillations in surface did not exceed 5%.

Thus, the source created local nonuniformities of the surface with given parameters: spanwise spacing, frequency and amplitude. The periodic form of nonuniformities in the spanwise direction (in the form of a standing wave) was chosen to provide an effective generation of periodic vortices in the boundary layer. Special tests did not detect bending or buckling of the membranes due to a difference of static pressures in the flow and in the pneumatic lines. However, due to a feature of the process of hardening of the glue, the membrane surface in neutral position was about 15 µm below the plate surface that resulted in a small periodic undulation in the spanwise direction z.

By varying the diameter and the spacing of the membranes, the spanwise wavelength of the surface disturbances and, consequently, the spanwise wavelength of the generated vortices can be changed. The sources with a diameter of membranes 3.62 ± 0.04 mm and 5.44 ± 0.05 mm for spacing between their centers 4 mm and 6 mm, respectively, were used. The neighboring membranes oscillated in antiphase.

Table 1: Values $h_{\max}$ at membrane oscillations (µm).

λ_z, mm	$f=2$	5	8	11	14 Hz
8		30.0±2.0	36.0±2.2	45.0±2.0	48.1±3.7
12	27.6±0.3	30.9±0.6	37.8±0.5	47.2±1.0	51.7±2.3

As a result, the source created a periodic nonuniformity of the plate surface in the spanwise direction with transverse periods $\lambda_z = 8$ mm and 12 mm respectively. The excited instability disturbances (the Görtler vortices) were close to the most growing downstream (see, e.g., [11]).

The values $h_{\max}$ of the measured maximum deviations of membranes from the neutral position during oscillations in time at chosen frequencies f are presented in Table 1. The measurements were performed using a non-contact optical displacement measuring device with a precision of 0.1 µm. It has been found that deviations of points of each membrane from the neutral position (in the cylindrical coordinate system related to the center of a membrane) with high accuracy can be described by the formula

$$h(r) = h_{\max} \sum_{n=0}^{3} c_n \left(\frac{2r}{d}\right)^{2n}, \quad |r| \le d/2, \tag{2.1}$$

where

$$\sum_{n=0}^{3} c_n = \sum_{n=1}^{3} n c_n = 0,$$

r is the distance from the center of the membrane and $c_2 = 1.9375$, -0.3101 and $c_3 = -0.4591$, 0.6534 for the membranes with $\lambda_z = 8$ and 12 mm, respectively.

For the numerical model of the source, we assume that the number of membranes in the z-direction is infinite, and they oscillate harmonically with the circular frequency $\omega = 2\pi f$ in the direction y vertical with respect to the plane of membrane with amplitudes defined by (2.1), the neighboring membranes being in antiphase. On performing at each x a decomposition of the source amplitude in the Fourier series for z, we select at each x a harmonic with the main wave number $\beta = 2\pi/\lambda_z$ and assume further that the source is a strip, points of which oscillate in the vertical direction as

$$y = H_{\beta\omega}(x) \cos(\beta z - \omega t) \tag{2.2}$$

with fixed values of ω and β, where $H_{\beta\omega}(x)$ is a nonnegative function in x.

2.3 Boundary-layer characteristics

The boundary-layer measurements described in [2] have shown that the main characteristics of the flow over the plate practically do not depend on the spanwise coordinates in the range of several wavelenghts λ_z, that is, the boundary layer can be treated essentially as two-dimensional. Moreover, due to a careful selection of the form and location of the adjustable wall bump and the other elements of the experimental setup described in Sect. 2.1, the streamwise pressure gradient in the boundary layer was close to zero.

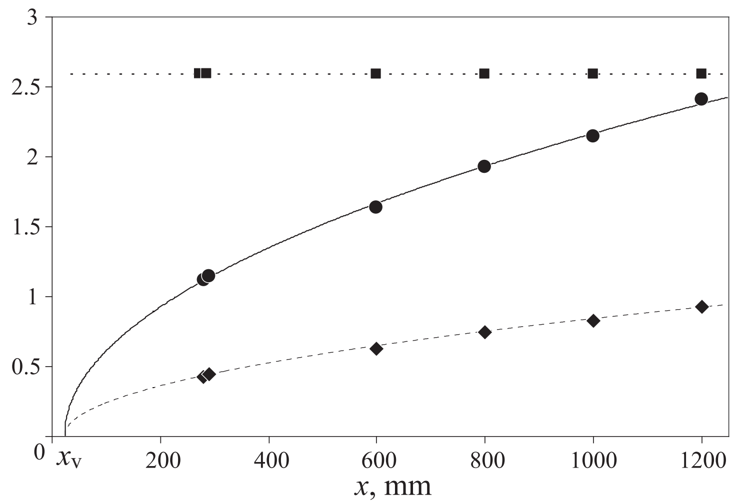

Figure 3: Comparison of integral boundary-layer characteristics. Experimental data [2]: δ^*, mm (●); δ^{**}, mm (⧫); δ^*/δ^{**} (■); numerical data for Blasius boundary layer (—), (−−), (···), respectively; the effective origin of the Blasius boundary-layer $x_v = 21.6$ mm.

The measured normal to the surface profiles of the streamwise velocity and corresponding integral characteristics of the base flow indicate that the boundary layer in the region of measurements was close to the Blasius one. The displacement thickness δ^*, momentum-loss thickness δ^{**}, and the shape factor δ^*/δ^{**} as functions of x are shown in Fig. 3 by symbols. As seen, they are in a good agreement with predictions for the Blasius boundary layer obtained numerically (shown by lines) if it is assumed that the Blasius boundary layer is formed downstream from $x = x_v$. This virtual Blasius boundary-layer origin was obtained by the least squares method to minimize the difference between the characteristics of the experimental boundary layer and the Blasius boundary layer.

2.4 Generation of controlled disturbances

A preliminary study [11] showed that the streamwise disturbance velocity component generated by the source has a maximum at a distance from the surface corresponding to the value of the dimensionless streamwise base velocity $U/U_e = 0.6 \pm 0.01$. Therefore, to minimize efforts, the measurements of amplitudes and phases of the perturbations were carried out at this distance from the surface.

The values of streamwise disturbance velocity component measured over a period were synchronised with a reference signal from the disturbance source and then ensemble averaged. The number of periods taken for the averaging varied from 20 to 210 depending on a regime of measurement (the streamwise velocity was measured for $10 \div 15$ s at each point of space). The sampling frequency of an analogue-to-digital converter was chosen to ensure a sufficiently large and always integer number of points per period of the generated signal. As a result, all obtained sequences of velocities were mutually synchronized in time and contained both amplitude and phase information. Then, these sequences were Fourier

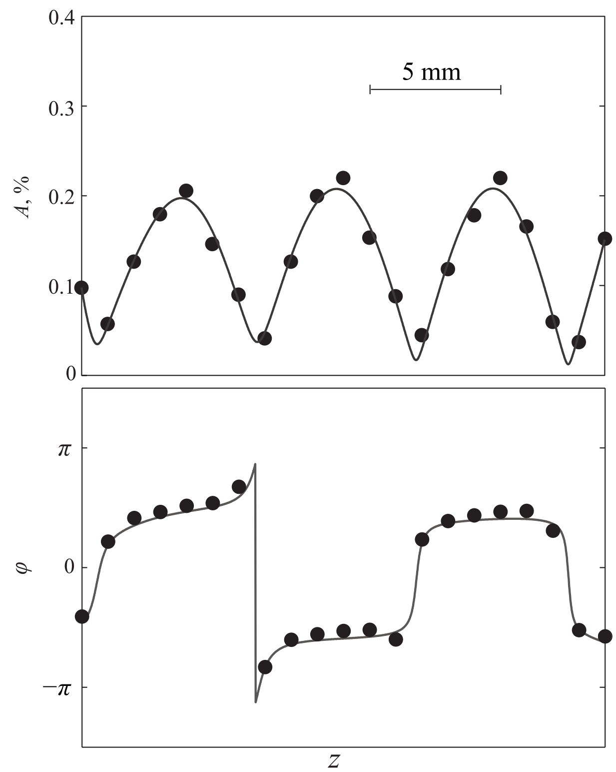

Figure 4: Amplitudes (*top*) and phases (*bottom*) of disturbances in z for $\lambda_z = 12$ mm and $f = 8$ Hz at $x = 1200$ mm): experimental data (•) and their approximation by a 10th-order polynomial (—) [2].

transformed in time in order to extract the information on amplitudes and phases of disturbances at the frequency of excitation f.

The experiments were carried out at frequencies of the vibrations of membranes $f = 2$, 5, 8, 11, and 14 Hz. The wavelength of excited Görtler vortices in the spanwise direction was either 8 or 12 mm. Figure 4 shows a typical behavior of the amplitude and phase of the streamwise disturbance velocity in z inside the boundary layer far downstream from the source (at the end of the examined interval in x). The observed dependencies are characteristic for a standing wave, indicating both the presence of a pair of Görtler vortices with the spanwise wavenumbers $\pm\beta$ and having the same frequency f and amplitude and the presence of a small admixture of other perturbations with multiple spanwise wavenumbers generated by the source. An analysis of disturbances with frequency $2f$ conducted to test the linearity of the source and evolution of disturbances showed the absence of significant deviations from linearity.

Fourier transform of the streamwise disturbance velocity in z made it possible to extract the amplitudes and phases of disturbances with the spanwise wavenumbers $\pm\beta$ as described in Sect. 2.2. These data are used in Sect. 3 for comparison with numerical results.

Examples of extracted in such a way profiles of amplitudes and phases in y-direction (at the location of one of the amplitude maxima in z as in Fig. 4) are shown by symbols in Fig. 5 for $x = 1200$ mm. The results of computations made in [11] for the conditions of the experiment using two variants of

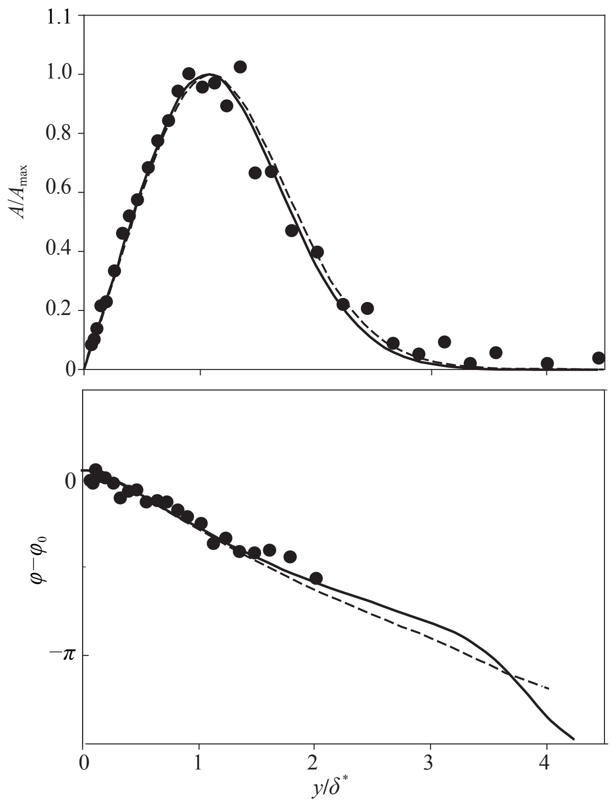

Figure 5: Amplitude (*top*) and phase (*bottom*) profiles obtained experimentally [2] (•) for $\lambda_z = 12$ mm $f = 8$ Hz at $x = 1200$ mm in comparison with the results of computations using linear theory of hydrodynamic stability with account for (—) and dropping (−−) the terms containing the velocity of the base flow normal to the surface V and streamwise derivatives of the streamwise velocity of the base flow U (see details in [11]).

the linearized evolution equations of Görtler vortex are shown by lines. As seen, the experimental and computed profiles are in a good agreement with each other.

3 Simulation using parabolic equations

In this section we will describe a simplified theoretical model based on parabolized equations. As mentioned in Sect. 1, this model is quite adequate for analysis of experimentally observed boundary-layer receptivity to local nonuniformities of flow-exposed surface at generation of the Görtler vortices and made it possible to build in [3] a new theory of receptivity based on optimal disturbances. However, in some cases, this model does not accurately simulate the streamwise disturbance velocity found in the experiment. The reason for this is still insufficiently understood.

3.1 Theoretical model

The controlled disturbances excited in the boundary layer in the experiments have very low amplitudes of several tenths or even hundredths of a percent of the mean flow velocity. Therefore, we assume that their generation and propagation downstream from the source is described with a good accuracy by linearized hydrodynamics equations.

Let us consider a slightly concave plate of infinite span placed under zero angle of attack into a uniform flow of a viscous incompressible fluid with velocity vector of length U_e, which is perpendicular to the plate leading edge. We assume that the radius $R > 0$ of the plate curvature is constant and significantly greater than the thickness δ of the boundary layer formed on the plate under the action of viscosity. Let us introduce the following notations: $x \geq 0$ is the streamwise coordinate (arc length along the plate surface counted from the leading edge), $y \geq 0$ is the wall-normal coordinate (a distance from the plate surface), z is the spanwise coordinate (along the leading edge of the plate), which is perpendicular to the (x, y)-plane, t is time. Let the flow which is formed over the plate in the absence of any disturbances be called the *base flow*. The velocity component of the base flow in the spanwise direction is equal to zero. The velocity components U and V in the x- and y-directions, respectively, and the pressure P do not depend on z and t.

Let the disturbance source be an oscillating impermeable membrane of streamwise width l extended infinitely in the z-direction and located downstream of the plate leading edge between coordinates $x_0 - l$ and x_0, where $x_0 \gg l$. Let us denote the velocity components and the pressure of the perturbed flow by $u(x, y, z, t)$, $v(x, y, z, t)$, $w(x, y, z, t)$, and $p(x, y, z, t)$, respectively. Using the boundary-layer normalization, we scale time by x_0/U_e; x and l by x_0; y, z, R and δ by $x_0/\sqrt{\mathrm{Re}}$; u by U_e; v and w by $U_\mathrm{e}/\sqrt{\mathrm{Re}}$; p by $\rho U_\mathrm{e}^2/\mathrm{Re}$, where $\mathrm{Re} = x_0 U_\mathrm{e}/\nu$ denotes the Reynolds number, ρ is the fluid density, and ν is the fluid kinematic viscosity. For dimensionless variables we keep the same notations.

In the considered case, when $R \gg \delta$, the base flow developed over the plate far downstream from its leading edge is assumed to satisfy the Blasius equations [6, 12, 13]:

$$U\frac{\partial U}{\partial x} + V\frac{\partial U}{\partial y} = \frac{\partial^2 U}{\partial y^2}, \quad \frac{\partial U}{\partial x} + \frac{\partial V}{\partial y} = 0, \tag{3.3}$$

with the following no-slip and free-stream boundary conditions:

$$U(x, 0) = V(x, 0) = 0, \quad U(x, \infty) = 1, \tag{3.4}$$

where, in accordance to the above scaling, $U(x, y)$ and $V(x, y)$ are the dimensionless streamwise and wall-normal velocity components.

The system of linear equations, describing the development of small-amplitude Görtler vortices in the two-dimensional boundary layer has the following form:

$$\begin{aligned}
\frac{\partial u'}{\partial t} + U\frac{\partial u'}{\partial x} + \frac{\partial U}{\partial x}u' + V\frac{\partial u'}{\partial y} + \frac{\partial U}{\partial y}v' &= \frac{\partial^2 u'}{\partial y^2} + \frac{\partial^2 u'}{\partial z^2}, \\
\frac{\partial v'}{\partial t} + U\frac{\partial v'}{\partial x} + \frac{\partial V}{\partial x}u' + V\frac{\partial v'}{\partial y} + \frac{\partial V}{\partial y}v' + 2\mathrm{G\ddot{o}}^2 U u' + \frac{\partial p'}{\partial y} &= \frac{\partial^2 v'}{\partial y^2} + \frac{\partial^2 v'}{\partial z^2}, \\
\frac{\partial w'}{\partial t} + U\frac{\partial w'}{\partial x} + V\frac{\partial w'}{\partial y} + \frac{\partial p'}{\partial z} &= \frac{\partial^2 w'}{\partial y^2} + \frac{\partial^2 w'}{\partial z^2}, \\
\frac{\partial u'}{\partial x} + \frac{\partial v'}{\partial y} + \frac{\partial w'}{\partial z} &= 0,
\end{aligned} \tag{3.5}$$

where $u' = u - U$, $v' = v - V$, $w' = w$, $p' = p - P$, and $\mathrm{G\ddot{o}}^2 = \sqrt{\mathrm{Re}/R}$ is the Görtler number. This system is derived from the full Navier–Stokes equations for viscous incompressible fluid in the curvilinear coordinates introduced above taking into account the smallness of the curvature and using linearization and parabolization in the streamwise direction by dropping viscous terms and the streamwise derivative of pressure, which are relatively small in the case of large Reynolds numbers [11, 14].

We will assume that there are no disturbances of the base flow upstream of the membrane, the no-slip conditions are satisfied on the plate surface downstream from the membrane, and the disturbances decay as $y \to \infty$. The boundary conditions on the membrane surface at $1 - l \le x \le 1$ require special consideration. Let the oscillating membrane undergo instantaneous shifts $\xi(x,z,t)$, $\eta(x,z,t)$, and $\zeta(x,z,t)$ about its neutral position along x, y, and z-axis, respectively. Then, the dynamic no-slip conditions take the form

$$\begin{aligned}
\frac{\partial \xi}{\partial t} &= u(x+\xi, \eta, z+\zeta, t), \\
\frac{\partial \eta}{\partial t} &= v(x+\xi, \eta, z+\zeta, t), \\
\frac{\partial \zeta}{\partial t} &= w(x+\xi, \eta, z+\zeta, t).
\end{aligned}$$

Assuming that both displacements and velocities of points of the membrane surface in the x- and z-directions are negligible, we expand the flow velocity components in the Taylor series near point $(x, 0, z)$, setting $\xi = \zeta = \partial\xi/\partial t = \partial\zeta/\partial t = 0$ and deleting the nonlinear (with respect to η) terms. As a result we obtain the following system of equations:

$$\begin{aligned}
0 &= u(x,0,z,t) + \frac{\partial u}{\partial y}(x,0,z,t)\eta, \\
\frac{\partial \eta}{\partial t} &= v(x,0,z,t) + \frac{\partial v}{\partial y}(x,0,z,t)\eta, \\
0 &= w(x,0,z,t) + \frac{\partial w}{\partial y}(x,0,z,t)\eta.
\end{aligned}$$

Taking into account that at $y = 0$ the velocity components of the base flow satisfy the equalities $U = V = 0$ and $\partial V/\partial y = -\partial U/\partial x = 0$ and deleting terms of the second order of smallness, we get, finally, the following linearized boundary conditions for the disturbance velocity components:

$$u'(x,0,z,t) = -\frac{\partial U}{\partial y}(x,0)\eta, \quad v'(x,0,z,t) = \frac{\partial \eta}{\partial t}, \quad w'(x,0,z,t) = 0, \quad 1 - l \le x \le 1.$$

The substantiation of such boundary conditions can be traced to [15] and, hence, they are called sometimes as Benjamin's boundary conditions. They are widely used, in particular, for studying various shear-flow instabilities near compliant coatings [17–19] and other surface nonuniformities in the cases of parallel and non-parallel flows [20, 21].

In conformity with the previous section, we assume further that the membrane oscillation is harmonic in z and t, i.e.

$$\eta(x,z,t) = \mathrm{real} H_{\beta\omega}(x) \mathrm{e}^{\mathrm{i}(\beta z - \omega t)},$$

where $\beta \neq 0$ and $\omega \geq 0$ are the real wavenumber and circular frequency, respectively, and $H_{\beta\omega}(x)$ is a scalar non-negative function which is identically equal to zero at $x \leq 1-l$ and $x \geq 1$. In this case, the solution of system (3.5) can be found in the following form:

$$\begin{pmatrix} u'(x,y,z,t) \\ v'(x,y,z,t) \\ w'(x,y,z,t) \\ p'(x,y,z,t) \end{pmatrix} = \mathrm{real} \begin{pmatrix} \bar{u}(x,y) \\ \bar{v}(x,y) \\ \bar{w}(x,y) \\ \bar{p}(x,y) \end{pmatrix} \mathrm{e}^{\mathrm{i}(\beta z - \omega t)}$$

and system (3.5) is reduced to a system of equations for the complex amplitudes of disturbances, which can be written in the following form:

$$\begin{aligned}
\frac{\partial \bar{u}}{\partial x} + \frac{\partial \bar{v}}{\partial y} + \mathrm{i}\beta \bar{w} &= 0, \\
\frac{\partial (U\bar{v} + V\bar{u})}{\partial x} + 2\frac{\partial V\bar{v}}{\partial y} + \mathrm{i}\beta V\bar{w} + 2\mathrm{G\ddot{o}}^2 U\bar{u} + \frac{\partial \bar{p}}{\partial y} &= \frac{\partial^2 \bar{v}}{\partial y^2} - \beta^2 \bar{v} + \mathrm{i}\omega \bar{v}, \\
\frac{\partial U\bar{w}}{\partial x} + \frac{\partial V\bar{w}}{\partial y} + \mathrm{i}\beta \bar{p} &= \frac{\partial^2 \bar{w}}{\partial y^2} - \beta^2 \bar{w} + \mathrm{i}\omega \bar{w}, \\
V\frac{\partial \bar{u}}{\partial y} - \frac{\partial V}{\partial y}\bar{u} + \frac{\partial U}{\partial y}\bar{v} - U\frac{\partial \bar{v}}{\partial y} - \mathrm{i}\beta U\bar{w} &= \frac{\partial^2 \bar{u}}{\partial y^2} - \beta^2 \bar{u} + \mathrm{i}\omega \bar{u}.
\end{aligned} \tag{3.6}$$

Note that the streamwise momentum equation (the last equation in (3.6)) differs from the conventional one, cf., e.g., eq. (3) in [11]. It was obtained by applying the continuity equations for the base flow and disturbances to remove x-derivatives in the streamwise momentum equation.

The initial conditions for the system (3.6) and the boundary conditions at $y = \infty$ have the form

$$\bar{u}(1-l,y) = \bar{v}(1-l,y) = \bar{w}(1-l,y) = \bar{p}(1-l,y) = 0 \tag{3.7}$$

and

$$\bar{u}(x,\infty) = \bar{v}(x,\infty) = \bar{w}(x,\infty) = 0,\ x \geq 1-l, \tag{3.8}$$

respectively, and the boundary conditions at $y = 0$ have the form

$$\begin{aligned}
\bar{u}(x,0) &= -\frac{\partial U}{\partial y}(x,0) H_{\beta\omega}(x), \\
\bar{v}(x,0) &= -\mathrm{i}\omega H_{\beta\omega}(x), \\
\bar{w}(x,0) &= 0,\ 1-l \leq x \leq 1,
\end{aligned} \tag{3.9}$$

and

$$\bar{u}(x,0) = \bar{v}(x,0) = \bar{w}(x,0) = 0, \ x > 1.$$

One has to emphasize that the usage of model (3.6)–(3.9) is justifiable at large Reynolds numbers: $\mathrm{Re} \gg 1/H_{\max}$, where

$$H_{\max} = \max H_{\beta\omega}(x),$$

small amplitudes of oscillations in respect to the boundary-layer thickness: $H_{\max} \ll \delta$, and at the boundary-layer thickness much smaller than the characteristic streamwise wavelength of the vortex [15]. All these conditions are satisfied in the present study.

3.2 Numerical model

For a discretization in the y-direction of system (3.6) with the initial conditions (3.7) and boundary conditions (3.8) and (3.9) we use the method of collocations. Let us take a sufficiently large $y_{\max} \gg \delta$ and replace the boundary conditions (3.8) for the amplitudes of the components of disturbance velocity by

$$\bar{u}(x, y_{\max}) = \bar{v}(x, y_{\max}) = \bar{w}(x, y_{\max}) = 0, \ x > 1 - l.$$

The adequacy of the choice of $y_{\max}$ will be analyzed *a posteriori* by the independence (within the specified accuracy) of the obtained results, as $y_{\max}$ is increased.

Let us make the following change of variables in equations (3.6):

$$y = y(s) = y_{\max} \frac{1+s}{2 + (1-s)\sigma}, \ -1 \le s \le 1,$$

where $\sigma > 0$ is a scaling factor, and choose the roots of the Chebyshev polynomial of the second kind $U_N(s)$ of degree N as nodes for interpolating the pressure in s, i.e.

$$s_j = \cos \frac{\pi j}{N+1}, \quad j = 1, \ldots, N, \tag{3.10}$$

and the same points and $s_0 = 1$ and $s_{N+1} = -1$ for interpolating the velocity components. Substituting into equations, obtained from (3.6) by means of this change of variables, interpolation polynomials, which approximate variables $\bar{u}$, $\bar{v}$, $\bar{w}$ and $\bar{p}$, requiring that the obtained equations hold at points (3.10), and using the methods described in [22] for computing the derivatives of polynomials at these points, we come to a system of ordinary differential and algebraic equations of the form

$$\begin{gathered} v(1-l) = 0, \ \frac{\mathrm{d}}{\mathrm{d}x} D(x) v = J(x) v + Gp + H(x) f_v(x), \\ F(x) v + H(x) f_p(x) = 0, \end{gathered} \tag{3.11}$$

with a scalar function $H(x) = H_{\beta\omega}(x)$ such that

$$H(1-l) = H(x) \equiv 0, \ x \ge 1, \tag{3.12}$$

where $v(x) \in \mathbf{C}^{n_v}$ and $p(x) \in \mathbf{C}^{n_p}$ are the vectors of values of the velocity components and pressure, respectively, at the internal nodes of the grid, $J(x) \in \mathbf{C}^{n_v \times n_v}$ and $F(x) \in \mathbf{C}^{n_p \times n_v}$ are matrices, and

$f_v(x) \in \mathbf{C}^{n_v}$, $f_p(x) \in \mathbf{C}^{n_p}$ are vectors that depend smoothly on x, $n_v = 3N$, $n_p = N$, and $G \in \mathbf{C}^{n_v \times n_p}$ is a matrix that is independent of x. Taking into account that $l \ll 1$ we consider further the base flow to be constant in the range of $1 - l \leq x \leq 1$, assuming

$$D(x) \equiv D(1),\ J(x) \equiv J(1),\ F(x) \equiv F(1),\ f(x) \equiv f(1),\ 1 - l \leq x \leq 1.$$

The matrices $D(x)$, $J(x)$, and $F(x)$ include the velocity components U and V of the base flow and their derivatives with respect to y at grid nodes $y(s_j)$. We compute $U(x, y(s_j))$ and $V(x, y(s_j))$ for $x = 1$ and then use these values as initial ones for computing U and V at the same grid nodes for $x > 1$ by the delaying coefficients method and the Crank–Nicolson scheme [23].

For computing $U(1, y(s_j))$ and $V(1, y(s_j))$ we need to solve the system (3.3), (3.4). Its solution can be represented in the self-similar form [13]:

$$U = \frac{\mathrm{d}g}{\mathrm{d}r}, \quad V = \frac{1}{2\sqrt{x}}\left(rU - g\right),$$

where g is a function of one variable $r = y/\sqrt{x}$, which satisfies the equation

$$2\frac{\mathrm{d}^3 g}{\mathrm{d}r^3} + g\frac{\mathrm{d}^2 g}{\mathrm{d}r^2} = 0$$

with the boundary conditions

$$g(0) = \frac{\mathrm{d}g}{\mathrm{d}r}(0) = 0, \quad \frac{\mathrm{d}g}{\mathrm{d}r}(\infty) = 1.$$

For computing g at the nodes $r_j = y(s_j)$ we use the method described in detail in [24, 25].

Applying an algebraic dimension reduction proposed in [26, 27] to the differential-algebraic initial-value problem (3.11) with the matrices and right-hand side that depend smoothly on x, one can show that the following conditions

$$\det D(x) \neq 0,\ \det F(x) D(x)^{-1} G \neq 0$$

make it possible to eliminate p and guarantee the existence and uniqueness of the solution.

Taking this result into account we will consider separately the generation of the disturbance $v^0 = v(1)$ by solving the initial-value problem

$$\begin{gathered} v(1-l) = 0,\ \frac{\mathrm{d}}{\mathrm{d}x} D(1) v = J(1) v + Gp + H(x) f_v(1), \\ F(1) v + H(x) f_p(1) = 0,\ 1 - l < x \leq 1, \end{gathered} \tag{3.13}$$

and the downstream propagation of the disturbance, by solving the initial-value problem

$$\begin{gathered} v(1) = v^0,\ \frac{\mathrm{d}}{\mathrm{d}x} D(x) v = J(x) v + Gp, \\ F(x) v = 0,\ x > 1. \end{gathered}$$

For approximating these initial-value problems in x, we will use the BDF2 method [28] with a fixed grid step.

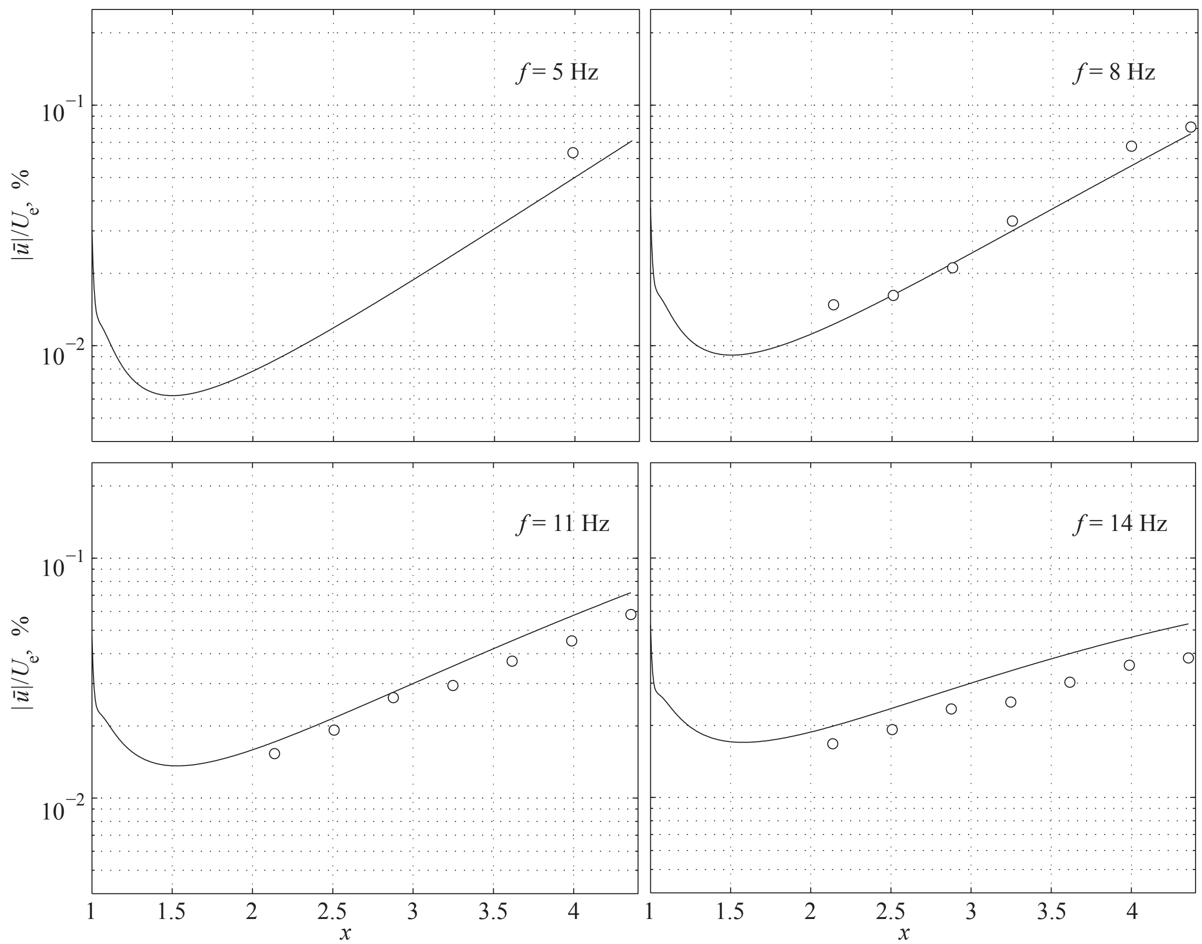

Figure 6: Computed (—) and measured (∘) amplification curves for amplitudes of the streamwise disturbance velocity at wall-normal distances corresponding to $U/U_\mathrm{e} = 0.6$ for $\lambda_z = 8$ mm.

3.3 Comparison with the experiment

Some results of the computations and measurements are presented and compared with each other in Figs 6 and 7 for two different values of the spanwise wavelength λ_z and for various values of the disturbance frequency f. The experimental and computed amplification curves for amplitudes of the streamwise disturbance velocity at wall-normal distances corresponding to $U/U_\mathrm{e} = 0.6$ are presented in the figures. As seen, the slope of amplitude curves far downstream from the source is simulated correctly. The difference in the amplitudes of the experimental and computed disturbances can be explained, most probably, by either an incomplete adequacy of the numerical model of the disturbance source or/and by some possible inaccuracy of the experimental results obtained after the data processing described above. Note that the underestimation of the computed disturbance amplitudes observed at low frequencies correlates well with the findings in work [29], in which an application of a linearized source model led to a similar effect compared with results of direct numerical simulation. Additionally, the boundary

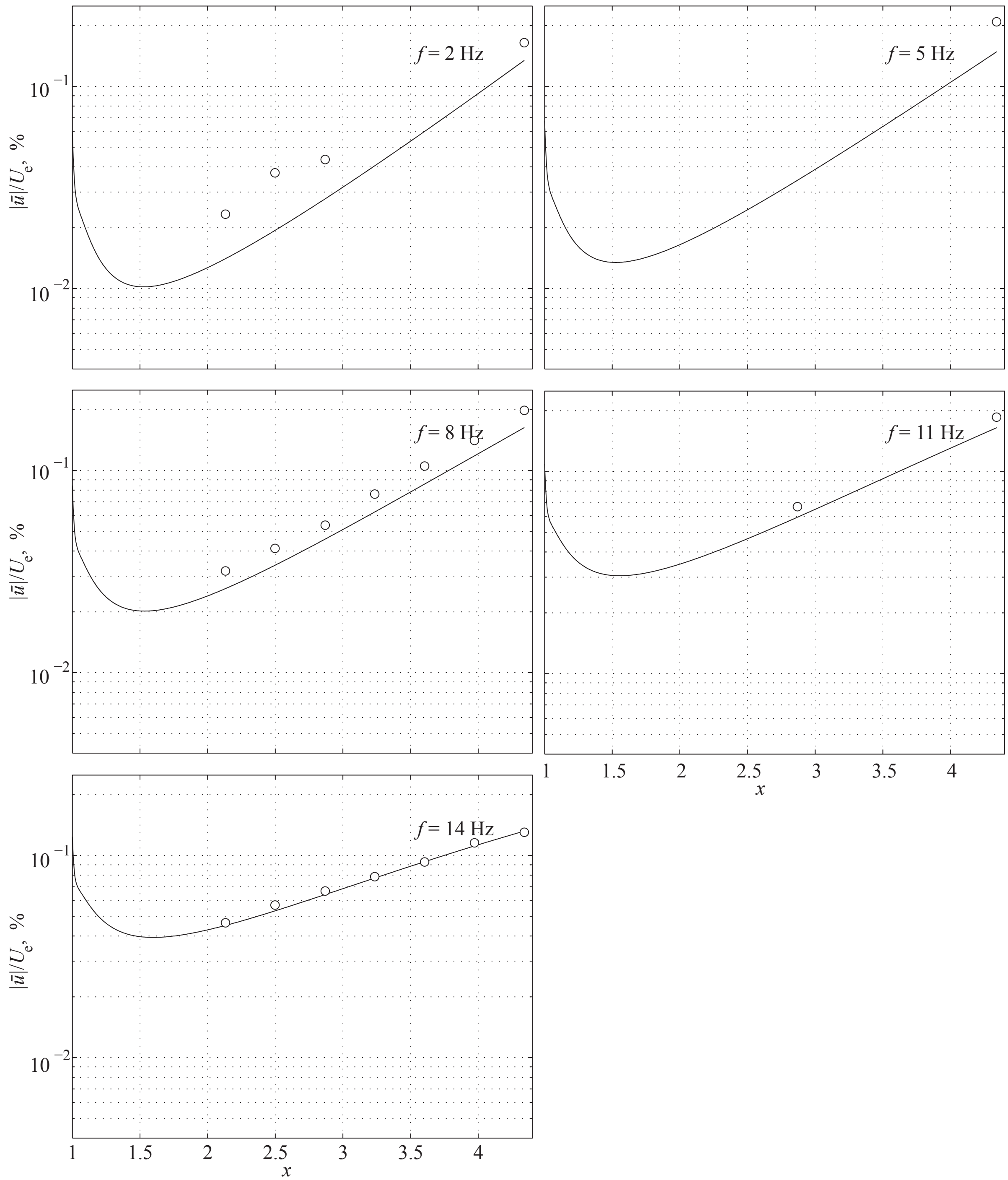

Figure 7: Computed (—) and measured (∘) amplification curves for amplitudes of the streamwise disturbance velocity at wall-normal distances corresponding to $U/U_\mathrm{e} = 0.6$ for $\lambda_z = 12$ mm.

Table 2: Parameters of computations with $\lambda_z = 8$ mm.

f, Hz	5	8	11	14
$H_{\max}$	0.0421	0.0507	0.0632	0.0677
Gö	3.6278	3.6332	3.6288	3.6308
β	0.5217	0.5202	0.5214	0.5209
ω	0.9257	1.4812	2.0366	2.5921
$\mathrm{Re} \times 10^{-5}$	1.6583	1.6682	1.6601	1.6638
l	0.0135	0.0135	0.0135	0.0135

Table 3: Parameters of computations with $\lambda_z = 12$ mm.

f, Hz	2	5	8	11	14
$H_{\max}$	0.0426	0.0478	0.0584	0.0730	0.0800
Gö	3.6427	3.6430	3.6430	3.6429	3.6428
β	0.3472	0.3472	0.3472	0.3472	0.3472
ω	0.3715	0.9288	1.4861	2.0433	2.6006
$\mathrm{Re} \times 10^{-5}$	1.6747	1.6752	1.6752	1.6751	1.6749
l	0.0200	0.0200	0.0200	0.0200	0.0200

conditions (3.9) are very sensitive at zero frequency to a particular state of the boundary layer near the surface, which can differ from the perfect Blasius boundary layer in the considered wind-tunnel experiment. As the frequency increases, the second boundary condition in (3.9), whose coefficients are controlled in the experiment very accurately, becomes dominant, that is, the relative role of $\partial U/\partial y$ at $y = 0$ in the vortex excitation becomes weaker. In the present case, the apparent 'attraction' of the experimental and numerical amplitude dependencies to each other at higher frequencies (for large spanwise wavelength, Fig. 7) supports this conjecture and indicates also that the linearized model of the boundary conditions works probably more accurately in the unsteady situation (at least for $\lambda_z = 12$ mm).

The described computations were performed for the following values of parameters: $y_{\max} = 30$, $\sigma = 11$, the number $N = 50$ of grid points in y direction, the number of grid points on the source in x direction and from $x = 1$ to $x = x_{\max}$ was chosen to be 2000 and 500, respectively, where $x_{\max} = 4.3561$ for $\lambda_z = 8$ and $x_{\max} = 4.3419$ for $\lambda_z = 12$. Reducing the grid size and increasing $y_{\max}$ did not lead to any visible changes in the results. The parameters of computations are given in Tables 2 and 3.

4 Direct numerical simulation

4.1 The FEATFLOW package

The software package FEATFLOW is a general purpose subroutine collection for simulating viscous incompressible fluid flows using high-performance computers. The results described in Sect. 4.2 were obtained with a version of the package for solving the incompressible Navier–Stokes equations

$$\begin{aligned} \frac{\partial \mathbf{u}}{\partial t} + (\mathbf{u}\cdot\nabla)\,\mathbf{u} &= -\nabla \mathrm{p} + \nu\Delta\mathbf{u}, \\ \nabla\cdot\mathbf{u} &= 0, \end{aligned} \tag{4.14}$$

in a bounded domain Ω. In the global Cartesian coordinates $\mathbf{u} = (\mathrm{u}, \mathrm{v}, \mathrm{w})^T$ is the velocity vector and its components in x, y and z directions, respectively, p is the normalized pressure (the pressure divided by the density), ν is the kinematic viscosity. Equations (4.14) are solved using the initial condition

$$\mathbf{u}(\mathbf{x}, t) = \mathbf{u}_0(\mathbf{x}), \qquad \mathbf{x} \in \Omega,$$

where $\mathbf{x} = (\mathrm{x}, \mathrm{y}, \mathrm{z})^T$ and $\mathbf{u}_0(\mathbf{x})$ is a given vector function.

On the boundary $\Gamma = \Gamma_1 \bigcup \Gamma_2 \bigcup \Gamma_3$ of the computational domain Ω the following boundary conditions are imposed:

$$\mathbf{u} = \mathbf{g}_1, \qquad \mathbf{x} \in \Gamma_1, \tag{4.15}$$

$$\mathbf{n}\cdot\mathbf{u} = \mathbf{g}_2, \qquad \mathbf{x} \in \Gamma_2, \tag{4.16}$$

$$-\mathrm{p}\mathbf{n} + \nu\,(\mathbf{n}\cdot\nabla)\,\mathbf{u} = \mathbf{g}_3, \qquad \mathbf{x} \in \Gamma_3, \tag{4.17}$$

where $\mathbf{n}$ is the unit outward normal to Γ, Γ_i $(i = 1, 2, 3)$ are some non-overlapping subsets of Γ, and $\mathbf{g}_i$ are given functions.

The finite element approach based on hexahedral elements is used for spatial discretization of problem (4.14). Continuous quadratic (P2) elements are used for the approximation of the velocity components, and discontinuous linear (P1) elements are used to approximate the pressure.

After the discretization in space, the following differential-algebraic system is obtained

$$\begin{aligned} &M\frac{\mathrm{d}\mathbf{u}}{\mathrm{d}t} + N(\mathbf{u})\mathbf{u} - L\mathbf{u} + B\mathrm{p} = 0, \\ &B^T\mathbf{u} = 0, \end{aligned} \tag{4.18}$$

where $\mathbf{u}$ and p are time-dependent discrete analogues of the velocity vector and the normalized pressure respectively, M is the mass matrix, $N(\mathbf{u})$ is a discrete analogue of the operator $\mathbf{u}\cdot\nabla$ in (4.14) being a matrix that depends on $\mathbf{u}$, and matrices L, B and $-B^T$ are discrete analogues of the Laplace operator multiplied by ν, the gradient operator and the divergence operator, respectively.

The FEATFLOW package uses one-step-θ-schemes (the first-order backward Euler scheme, with $\theta = 1$, or the second-order Crank–Nicolson scheme, with $\theta = 1/2$), or fractional-step-θ-schemes [30, 31] for the discretization of time derivatives in (4.18). The use of the backward Euler scheme on each time step leads to the following nonlinear problem

$$\begin{aligned} &M\frac{\mathbf{u}^k - \mathbf{u}^{k-1}}{\tau} + N(\mathbf{u}^k)\mathbf{u}^k - L\mathbf{u}^k + B\mathrm{p}^k = 0, \\ &B^T\mathbf{u}^k = 0, \end{aligned} \tag{4.19}$$

for $\mathbf{u}^k$ and p^k, where τ is a time step. Using the following notation

$$A(\mathbf{u}) = M + \tau\left(N(\mathbf{u}) - L\right), \tag{4.20}$$

problem (4.19) can be written as

$$\begin{aligned} &A(\mathbf{u}^k)\mathbf{u}^k + \tau B\mathrm{p}^k = M\mathbf{u}^{k-1}, \\ &B^T\mathbf{u}^k = 0. \end{aligned} \tag{4.21}$$

To solve (4.21), the FEATFLOW package uses a projection scheme explained, e.g., in [30–32]. Its main steps are summarized below:

— choose some $\tilde{\mathrm{p}}$, e.g., $\tilde{\mathrm{p}} = \mathrm{p}^{k-1}$;

— solve for $\tilde{\mathbf{u}}$ the following nonlinear system

$$A(\tilde{\mathbf{u}})\tilde{\mathbf{u}} + \tau B\tilde{\mathrm{p}} = M\mathbf{u}^{k-1}, \tag{4.22}$$

using, e.g., the Newton method;

— using $\tilde{\mathbf{u}}$, solve for $\mathrm{p}^k - \tilde{\mathrm{p}}$ the following system

$$\tau B^T M_L^{-1} B(\mathrm{p}^k - \tilde{\mathrm{p}}) = B^T\tilde{\mathbf{u}} \tag{4.23}$$

with $M_L \approx A(\tilde{\mathbf{u}})$;

— set

$$\mathbf{u}^k = \tilde{\mathbf{u}} - \tau M_L^{-1} B(\mathrm{p}^k - \tilde{\mathrm{p}}).$$

If necessary, the above steps may be repeated with $\tilde{\mathrm{p}} = \mathrm{p}^k$. It can be shown that the resulting solution $\mathbf{u}^k$ satisfies the discrete continuity equation $B^T\mathbf{u}^k = 0$.

If τ is small enough, then (4.20) implies $A(\tilde{\mathbf{u}}) \approx M$. In this case, in the capacity of M_L, the FEATFLOW package uses a diagonal matrix such that the i-th nonzero diagonal element is equal to the sum of the elements of the i-th row of matrix M.

The projection scheme described above is proposed in [33] for solving nonlinear problems of the form (4.21). At sufficiently small τ, that is, with a dominance of the mass matrix in the operator (4.20) and with a good initial guess, the computation of the solution at a new time step requires generally only a few iterations of this scheme [31, 32] (only one iteration in the computations described in Sect. 4.2). In applications to non-stationary problems, the solution from the previous time step provides a good initial guess. A version of the algorithm efficient for quite large time steps is discussed in [31].

The FEATFLOW package uses multigrid solvers for linear subproblems arising in the described projection scheme. Methods based on Gauss–Seidel or incomplete LU decomposition are used as smoothers. In particular, in the computations described in Sect. 4.2, the method of successive over-relaxation is used. To solve linear systems on a coarse mesh the method of successive over-relaxation is used for solving equation (4.22), while some direct solvers included in UMFPACK and based on the unsymmetrical multifrontal method [35, 36] are used for solving equation (4.23).

4.2 Base flow simulation

Let us consider a slightly concave plate with the radius of curvature $R = 8.370$ m placed under zero angle of attack into a uniform flow of a viscous incompressible fluid with the velocity vector $\mathbf{U}_\mathrm{e} = (\mathrm{U}_\mathrm{e}, 0, 0)^T$ of length $\mathrm{U}_\mathrm{e} = 9.18$ m/s which is perpendicular to the plate leading edge and the density $\rho = 1.214$ kg/m^3. This subsection is devoted to results of the computation of laminar boundary layers formed over the plate at different values of the dynamic viscosity μ and, therefore the kinematic viscosity $\nu = \mu/\rho$.

Let us introduce the Cartesian coordinates $(\mathrm{x}, \mathrm{y}, \mathrm{z})$, where x is the longitudinal direction, y is the vertical direction and z is the transverse direction. Two computational domains with and without buffer zones were implemented and tested. Figure 8 shows the computational domain with two buffer zones. The part of the bottom boundary of the computational domain coinciding with the plate surface (marked by dark-grey color) is denoted by Γ_{wall}. In the longitudinal direction x the plate is placed between two buffer zones. The left face Γ_{in} of the computational domain is an inflow boundary where the velocity vector $\mathbf{U}_\mathrm{e}$ is imposed, whereas the right face Γ_{out} of the computational domain is an outflow boundary where the so-called 'do-nothing' condition is used (equation (4.17) with $\mathbf{g}_3 = 0$). The no-slip (equation (4.15) with $\mathbf{g}_1 = 0$) and the no-penetration (equation (4.16) with $\mathbf{g}_2 = 0$) boundary conditions are satisfied on the plate surface and in the rest of the boundary of the computational domain, respectively.

The main problem, which had been encountered during the computations, was an appearance of spurious disturbances which developed in time in the vicinity of the plate leading and rear edges (marked by red dashed lines). To prevent appearance of such disturbances, a significant refinement of the mesh in the vertical and longitudinal directions near these edges (including the buffer zones) was necessary. However, even the mesh cells of length about 75 µm in the longitudinal and vertical directions did not allow to get rid of spurious velocity disturbances at $\mu = 10^{-4}$ Pa · s.

Figure 9 shows the computational domain without buffer zones. Instead of $\mathbf{U}_\mathrm{e}$, the velocity vector $\mathbf{U}_\mathrm{B} = (\mathrm{U}_\mathrm{B}, 0, 0)^T$ is set on the boundary Γ_{in}, where U_B is the streamwise Blasius boundary-layer velocity component. The component U_B was chosen to be equal to that of the perfect Blasius boundary-layer at a distance l_B from the leading edge. In addition, the outflow boundary Γ_{out} was replaced by the one that formed a right angle with the plate Γ_{wall}. Numerical experiments have shown that the removal of the buffer zones, the implementation of the new boundary condition on Γ_{in} and the 'rotation' of the outflow boundary Γ_{out} made it possible to significantly reduce the spurious velocity disturbances.

The results of the boundary layer computation at $\mu = 5 \times 10^{-5}$ Pa · s and $l_\mathrm{B} = 100$ mm for the plate of about 1650 mm long and 25 mm wide in the computational domain of 3000 mm height are given below. The computations were performed using the mesh mentioned in the previous subsection, with the cell size in the boundary layer approximately equal to 1.6 mm × 75 µm×3 mm in the longitudinal, vertical and transverse directions, respectively. Figure 10 shows the streamlines and the contour lines of the flow velocity which has been established over the plate. It is seen that near the plate surface the streamlines follow the shape of the surface, but at a distance of about 2000 mm they become almost

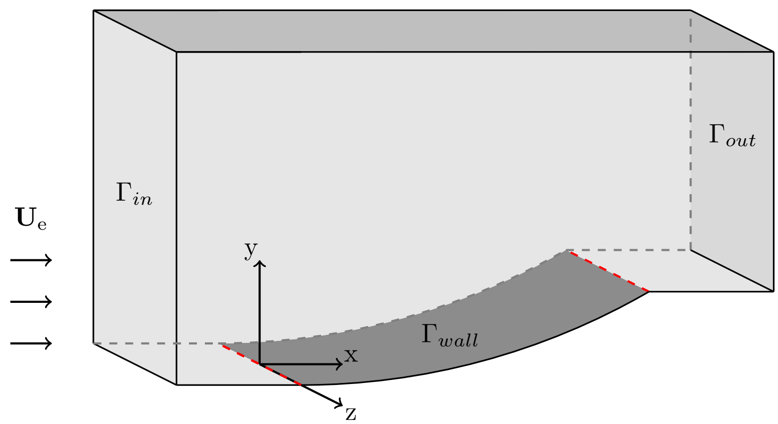

Figure 8: The computational domain with two buffer zones.

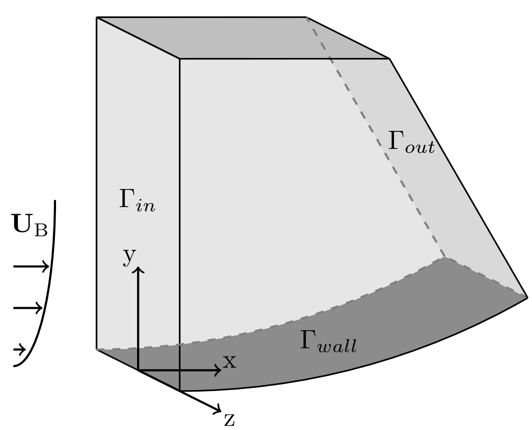

Figure 9: The computational domain without buffer zones.

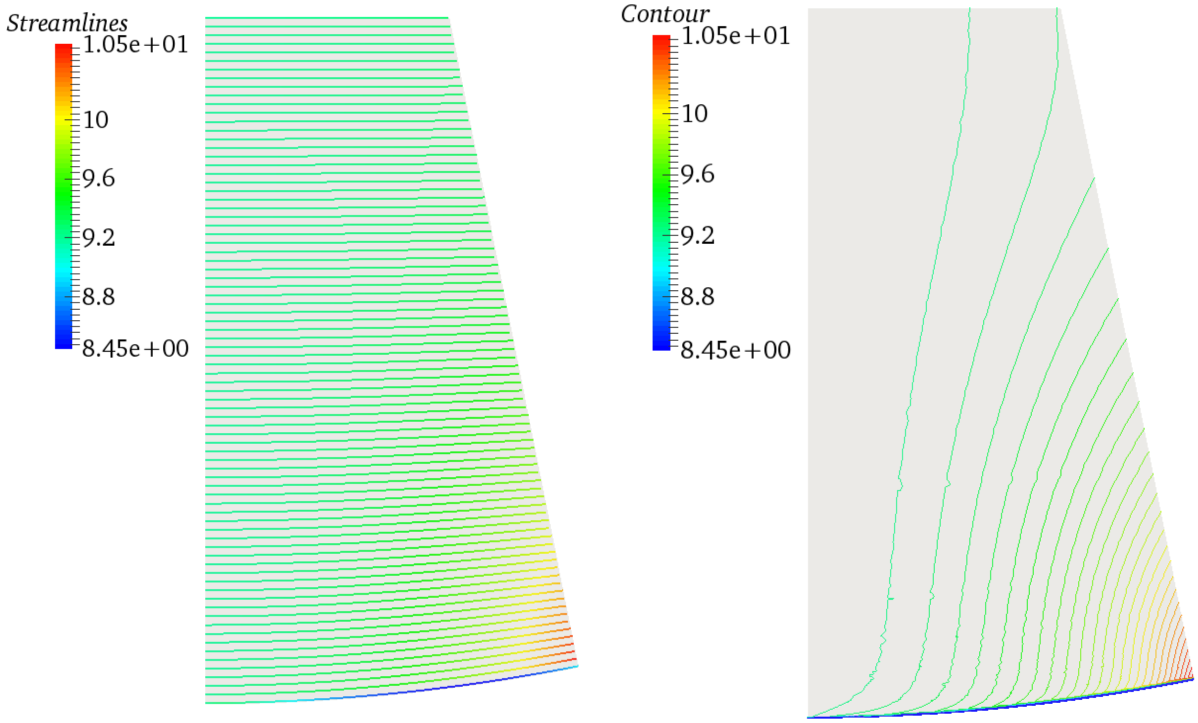

Figure 10: Streamlines (*left*), contour lines (*right*).

horizontal. The behavior of the streamlines and the contour lines indicates some acceleration of the fluid in the computational domain.

To analyze the computed boundary layer, the curvilinear coordinates x, y, z associated with the concave plate and described in Sect. 2.1 were used. At the same time, it was assumed that the Blasius boundary layer used as a reference flow to compare the results obtained with the FEATFLOW package, starts to develop at $x = 0$ that corresponds to the point $x = x_{\text{v}}$ in the wind-tunnel experiment.

Uniform meshes were used in x and z with 500 and 5 nodes, respectively. The mesh described in Sect. 3.2 was used in y with the number of inner nodes $N = 120$ and the following parameters: $\sigma = 8$ and $y_{\max} \approx 180$ mm. The velocity and pressure fields computed with the FEATFLOW package were interpolated on the introduced mesh with $500 \times 122 \times 5$ nodes and the velocity vector components U, V and W in the x, y, and z directions, respectively, were computed.

Figure 11 shows the streamwise component U vs. the self-similar variable

$$r = y\sqrt{\frac{\max\limits_{y}(U(x, y, z))}{2\nu x}}.$$

The top figure shows the dependencies $U(r)$ computed at different distances from the plate leading edge x for $z = 0$. As seen, at $x \leq 900$ mm the component U is self-similar with a good precision. The bottom figure shows the dependencies $U(r)$ at $x \approx 700$ mm and $-12.5 \leq z \leq 12.5$ (mm). It can be seen that the streamwise velocity component is constant in spanwise direction. So further we will discuss the results which correspond to $z = 0$.

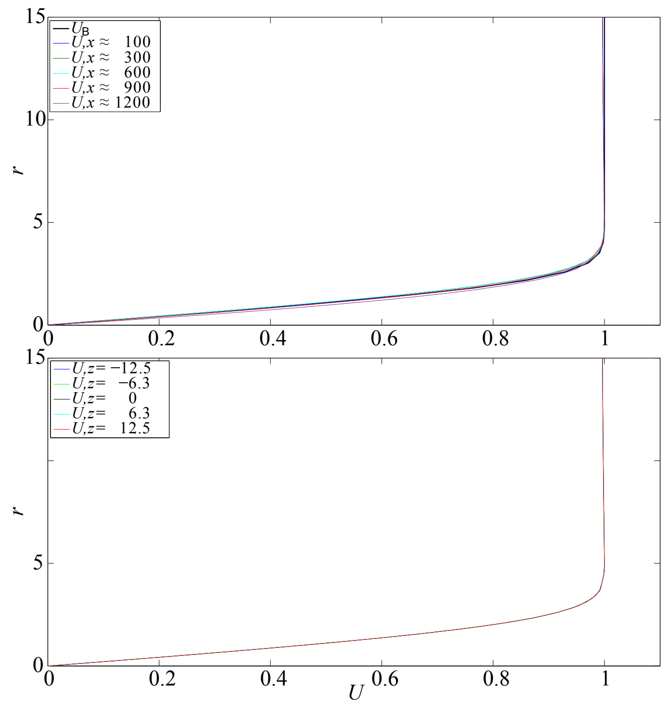

Figure 11: The dependencies of the streamwise component U on r at: different coordinates x, mm for $z = 0$ (*top*) and $x \approx 700$ mm and different z, mm (*bottom*).

Figure 12 shows the dependencies on x of squares of the displacement thickness δ^* and the momentum loss thickness δ^{**}, which are computed as follows

$$\delta^*(x) = \int\limits_0^{y_m(x)} \left(1 - \frac{U(x,y,0)}{U_m(x)}\right) \mathrm{d}y, \quad \delta^{**}(x) = \int\limits_0^{y_m(x)} \frac{U(x,y,0)}{U_m(x)} \left(1 - \frac{U(x,y,0)}{U_m(x)}\right) \mathrm{d}y,$$

where $y_m(x)$ is a minimum value of y at which $U(x,y,0)$ reaches its maximum

$$U_m(x) = \max_y U(x,y,0),$$

as well as squares of the corresponding Reynolds numbers. The dependencies corresponding to the Blasius boundary layer over a flat plate are highlighted in black while the dependencies corresponding to the boundary layer over the concave plate at different l_{B} are highlighted in green and red. It is seen that at $x \leq 750$ mm the dependencies associated with the boundary layer over the concave plate are quite close to linear as it should be in the case of a boundary layer which is close to self-similar one.

Figure 13 shows the dependence of the ratio of the displacement thickness and the momentum loss thickness (the so-called boundary-layer shape factor) on x (*left*), as well as the dependence of dimensionless pressure on x (*right*). It is seen that the value of shape factor begins to significantly deviate from the value 2.59, which is typical for the Blasius boundary layer, at $x \approx 600$ mm, and the increase of l_{B} by a factor of two does not change significantly the interval in which the shape factor is close to 2.59.

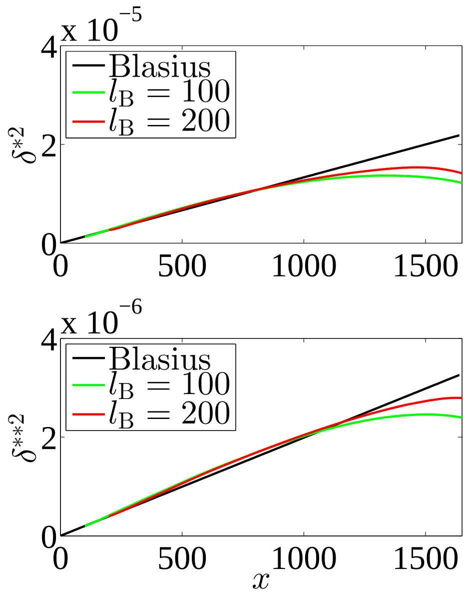

Figure 12: The dependencies on x of squares of the displacement thickness δ^* and the momentum loss thickness δ^{**} (*left*). The dependencies on x of corresponding squares of the Reynolds numbers Re_{δ^*} and $\mathrm{Re}_{\delta^{**}}$ (*right*).

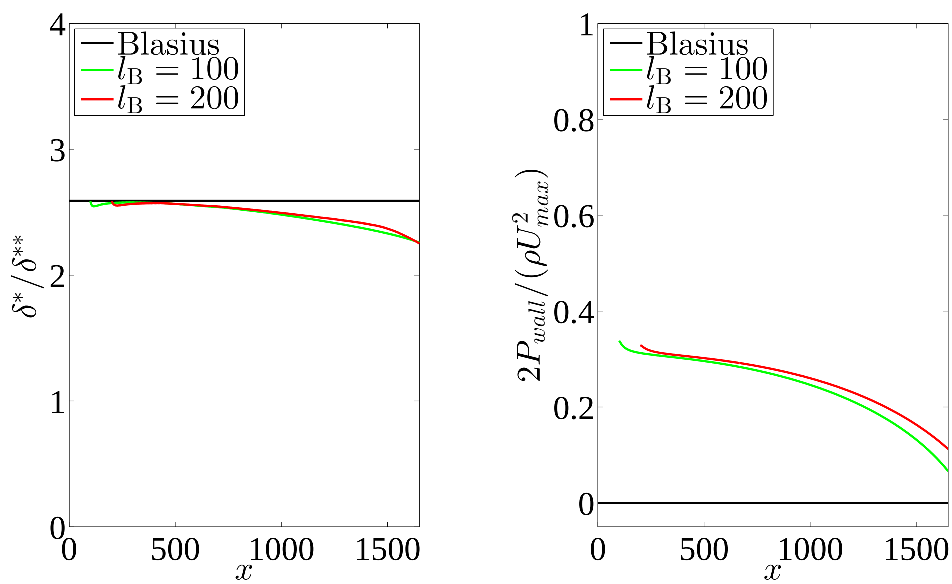

Figure 13: The ratio of the displacement thickness and the momentum loss thickness (*left*). Dimensionless pressure (*right*).

Thus, the use of the computational domain without buffer zones allows to obtain the flow close to self-similar in a significant region over the curved plate. Adjusting the shape of the upper wall and the boundary conditions on it as well as the size of the computational domain, apparently, may expand this region. At the same time, further increase of l_{B} is unlikely to be justified.

4.3 Simulation of controlled disturbances

The direct numerical simulation of the considered wind-tunnel experiment along with the appropriate simulation of the base flow requires an adequate simulation of the disturbance source, which is a rectangular part of the plate surface (the membrane) oscillating according to the law (2.1). To this end, it is advisable to choose the computational domain (see Fig. 9) of thickness 8 or 12 mm, equal to the wavelength $\lambda_z = 2\pi/\beta$ vibrations of the membrane in the transverse direction, and use the periodic boundary conditions on the side walls.

There is a number of studies, in which small nonuniformities of the surface are modeled by linearized boundary conditions, similar to those used in Sect. 3, but the adequacy of this approach is questionable. Among the studies devoted to the modeling of small surface disturbances by the linearized boundary conditions, the following ones should be noted:

— the pioneering works of Benjamin [15, 37–39], where linearized boundary conditions were proposed to model surface disturbances;

— work [16], where linearized boundary conditions for a stationary case of Görtler instability are discussed on pp. 346–347;

— work [40], where this approach is used and its adequacy is analyzed.

No detailed comparison of simulations using the linearized boundary conditions with results of physical experiments is available to date. Therefore, it seems reasonable to begin with modeling the disturbance source using the linearized boundary conditions (written in curvilinear coordinates)

$$\begin{aligned} u(x,0,z,t) &= -\frac{\partial U}{\partial y}(x,0)H_{\beta\omega}(x)\cos(\beta z - \omega t), \\ v(x,0,z,t) &= \omega H_{\beta\omega}(x)\sin(\beta z - \omega t), \\ w(x,0,z,t) &= 0. \end{aligned}$$

For non-linear simulation of the source, the following three approaches can be used:

— physical displacement of the boundary nodes, using the arbitrary Lagrangian–Eulerian (ALE) formulation of the Navier–Stokes equations. As the source is small in the longitudinal direction, one may need to simulate the generation of disturbances by solving local problems on a subgrid and transmitting forces/residuals to the coarse grid solver. This is feasible but would require major changes in the FEATFLOW package.

— the use of wall functions for natural (flux type) boundary conditions to model the source-induced disturbances in the variational formulation of the Navier–Stokes equations.

— modeling the source by adding extra terms to the continuity equation in boundary elements. The divergence of the velocity field is described by the volume change. The movement of the membrane changes the volume of the grid cells adjacent to the source. Instead of moving mesh nodes and recalculating the matrices obtained with the finite element discretization one can introduce terms describing the corresponding change of volume and its effect on the flow by 'blowing' or 'sucking' fluid into/from the boundaries of cells containing the source of disturbances.

5 Conclusion

The main problem with direct numerical simulation of wind-tunnel experiments using the FEATFLOW package is the absence of any stabilization in the version of this package based on high-order elements, which was used to obtain the results described in the previous section, and the use of low-order stabilization in the standard version of the package based on low-order elements proposed in [41].

To reach sufficiently high Reynolds numbers and improve robustness, it is necessary to develop and implement advanced high-order stabilization techniques to eliminate spurious oscillations, while preserving the physical disturbances under consideration. This is the main mathematical problem to be solved when it comes to creating a new branch of the FEATFLOW package intended for numerical simulation of experiments on stability of subsonic laminar shear flows in low-turbulence wind tunnels. In addition, it may be necessary

— to implement periodic boundary conditions in the transverse direction;

— to implement the slip condition on curved surfaces, which would reduce the computational cost when using a curved upper wall of the computational domain to eliminate a 'preload';

— to investigate how the currently used 'do-nothing' outflow boundary conditions affect the flow in the boundary layer and to look into the possibility of using more adequate outlet conditions, e.g., those proposed in [42];

— to develop and implement a model of the source based on the approaches described in Sect. 4.3.

Acknowledgments

This research was supported by the German Research Association (DFG) under grant KU 1530/18-1.

References

[1] *Ivanov A. V., Kachanov Y. S., Mischenko D. A.* Excitation of unsteady Görtler vortices by surface non-uniformities. Euromech Fluid Mechanics Conference – 8 (EFMC–8), September 13–16, 2010, Bad-Reichenhall, Germany. Abstracts. P. 4–12.

[2] *Ivanov A. V., Kachanov Y. S., Mischenko D. A.* Generation of nonstationary Görtler vortices by localized surface nonuniformities. receptivity coefficients. Thermophys. Aeromech. 2012. Vol. 19, No. 4, P. 523–539.

[3] *Boiko A. V., Ivanov A. V., Kachanov Y. S., Mischenko D. A., Nechepurenko Y. M.* Excitation of unsteady Goertler vortices by localized surface nonuniformities. Theor. Comput. Fluid Dyn. (submitted in 2015).

[4] *Drazin P. G., Reid W. H.* Hydrodynamic Stability. 2nd edn. Cambridge: Cambridge University Press, 2004. 628 p.

[5] *Floryan J. M.* On the Görtler instability of boundary layers. J. Aerosp. Sci. 1991. Vol. 28. P. 235–271.

[6] *Floryan J. M., Saric W. S.* Stability of Görtler vortices in boundary layers. AIAA J. 1982. Vol. 20, No. 3. P. 316–324.

[7] *Hall P.* Görtler vortices in growing boundary layers: The leading edge receptivity problem, linear growth and the nonlinear breakdown stage. Mathematika. 1990. Vol. 37. P. 151–189.

[8] *Saric W. S.* Görtler vortices. Annu. Rev. Fluid Mech. 1994. Vol. 26. P. 379–409.

[9] *Finnis M. V., Brown A.* The linear growth of Görtler vortices. Intern. J. Heat Fluid Flow. 1997. Vol. 18, No. 4. P. 389–399.

[10] *Bippes H.,Görtler H.* Dreidimensionale Störungen in der Grenzschicht an einer konkaven Wand. Acta Mech. 1972. Vol. 14. P. 251–267.

[11] *Boiko A. V., Ivanov A. V., Kachanov Y. S., Mischenko D. A.* Steady and unsteady Görtler boundary-layer instability on concave wall. Eur. J. Mech. – B/Fluids. 2010. Vol. 29, No. 2. P. 61-83.

[12] *Murphy J. S.* Extensions of the Falkner–Skan similar solutions to flows with surface curvature. AIAA J. 1965. Vol. 3, No. 11. P. 2043–2049.

[13] *Schlichting H., Gersten K.* Boundary layer theory, 8 edn. Berlin: Springer–Verlag, 2000. 800 p.

[14] *Hall P.* The linear development of Görtler vortices in growing boundary layers. J. Fluid Mech. 1983. Vol. 130. P. 41–58.

[15] *Benjamin T. B.* Shearing flow over a wavy boundary. J. Fluid Mech. 1959. Vol. 6, No. 2. P. 161–205.

[16] *Bottaro A., Zebib A.* Görtler vortices promoted by wall roughness. Fluid. Dyn. Res. 1997. Vol. 19, No. 6. P. 343–362.

[17] *Yeo K. S.* The stability of boundary-layer flow over single-and multi-layer viscoelastic walls. J. Fluid Mech. 1988. Vol. 196. P. 359–408.

[18] *Gaurav, Shankar V.* Stability of pressure-driven flow in a deformable neo-Hookean channel. J. Fluid Mech. 2010. Vol. 659. P. 318–350.

[19] *Hoepffner J., Bottaro A., Favier J.* Mechanisms of non-modal energy amplification in channel flow between compliant walls. J. Fluid Mech. 2010. Vol. 642. P. 489–507.

[20] *Tempelmann D., Schrader L. U., Hanifi A., Brandt L., Henningson D. S.* Swept wing boundary-layer receptivity to localized surface roughness. J. Fluid Mech. 2012. Vol. 711. P. 516–544.

[21] *Luchini P.* Linearized no-slip boundary conditions at a rough surface. J. Fluid Mech. 2013. Vol. 737. P. 349–367.

[22] *Weideman J. A. C., Reddy S. C.* A MATLAB differentiation matrix suite. ACM Trans. Math. Software. 2000. Vol. 26, No. 4. P. 465–519.

[23] *Tannehill J. C., Anderson D. A., Pletcher R. H.* Computational fluid mechanics and heat transfer, 3 edn. Series in Computational and Physical Processes in Mechanics and Thermal Sciences. CRC Press, 2012. 774 p.

[24] *Kierzenka J., Shampine L. F.* A BVP solver based on residual control and the Matlab PSE. ACM TOMS. 2001. Vol. 27, No. 3. P. 299–316.

[25] *Shampine L.F., Gladwell I., Thompson S.* Solving ODEs with MATLAB. Cambridge: Cambridge University Press, 2003. 263 p.

[26] *Boiko A. V., Nechepurenko Y. M.* Numerical spectral analysis of temporal stability of laminar duct flows with constant cross-sections. Comput. Math. Math. Phys. 2008. Vol. 48, No. 10. P. 1699–1714.

[27] *Nechepurenko Y. M.* On the dimension reduction of linear differential-algebraic control systems. Doklady Math. 2012. Vol. 86, No. 1. P. 457–459.

[28] *Hairer E., Nørsett S. P., Wanner G.* Solving ordinary differential equations I: Nonstiff Problems, 2nd edn. Berlin: Springer–Verlag, 2008. 528 p.

[29] *Schrader L.-U., Brandt L., Zaki T. A.* Receptivity, instability and breakdown of Görtler flow. J. Fluid Mech. 2011. Vol. 682. P. 362–396.

[30] *Turek S., Becker Chr.* Finite element software for the incompressible Navier-Stokes equations. User manual. Release 1.1. Heidelberg: Heidelberg University, 1998. 72 p.

[31] *Turek S.* Efficient solvers for incompressible flow problems: An algorithmic approach in view of computational aspects. LNCSE 2. Springer-Verlag, 1998.

[32] *Kuzmin D., Hämäläinen J.* Finite Element Methods for Computational Fluid Dynamics: A Practical Guide. SIAM, Philadelphia, 2014. 313 p.

[33] *Turek S., Kuzmin D.* Algebraic flux correction III. Incompressible flow problems. In: D. Kuzmin, R. Löhner and S. Turek (eds.) Flux-Corrected Transport: Principles, Algorithms, and Applications. 2nd edn. Springer Berlin Heidelberg, 2012. P. 251-296.

[34] *Davis T. A.* UMFPACK Version 5.3.0 User Guide. Gainesville: University of Florida, 2011. 140 p.

[35] *Davis T. A., Duff I. S.* An unsymmetric-pattern multifrontal method for sparse LU factorization. SIAM J. Matrix Anal. Applic. 1997. Vol. 18, No. 1. P. 140–158.

[36] *Davis T. A., Duff I. S.* A combined unifrontal/multifrontal method for unsymmetric sparse matrices. ACM Trans. Math. Softw. 1999. Vol. 25, No. 1. P. 1–19.

[37] *Benjamin T. B.* Effects of a flexible boundary on hydrodynamic stability. J. Fluid Mech. 1960. Vol. 9, No. 4. P. 513–532.

[38] *Benjamin T. B.* The development of three-dimensional disturbances in an unstable film of liquid flowing down an inclined plane. J. Fluid Mech. 1961. Vol. 10, No. 3. P. 401–419.

[39] *Benjamin T. B.* The threefold classification of unstable disturbances in flexible surfaces bounding inviscid flows. J. Fluid Mech. 1963. Vol. 16, No. 3. P. 436–450.

[40] *Voropayev G. A., Zagumennyi I. V.* Wave and vortex structure of the transitional boundary layer over a deformable surface. Phys. Scripta. 2010. Vol. 2010, No. 142. P. 1–9.

[41] *Rannacher R., Turek S.* A simple nonconforming quadrilateral Stokes element. Numer. Meth. Part. Diff. Equ. 1992. Vol. 8, P. 97-111.

[42] *Braack M., Mucha P.B.* Directional do-nothing condition for the Navier–Stokes equations. J. Comput. Math. 2014. Vol. 32, No. 5. P. 507–521.